Interfacial Effects on the Dielectric Properties of Elastomer Composites and Nanocomposites

Bo Li, Georgios Polizos, and Evangelos Manias

Abstract Elastomer-based composites and nanocomposites are discussed, with the emphasis on the filler and interfacial effects on their dynamics, and the resulting manifestation in their macroscopic dielectric or mechanical response. Specifically, selected polydimethylsiloxane (PDMS)/barium-titanate and styrene-butadiene rubber (SBR)/graphene oxide nanocomposites are discussed, as examples where controlled spatial distribution of filler (structured composites) gives rise to significantly different dielectric and thermomechanical behaviors. Also, ethylene–propylene–diene (EPDM)/carbon black (CB) composites are presented, as examples of systems that exhibit an abnormal temperature dependence of dielectric relaxation; and this response is discussed in the context of CB cluster polarization and quantified through a simple scaling model of the same. Finally, multi-filler EPDM/CB/ceramic elastomer nanocomposites are discussed, as examples of systems with antagonistic interfacial effects between conductive and dielectric fillers, as well as with strong interphase responses that can overwhelm the dielectric contributions from the fillers; in these systems, interphasial responses result in counter-intuitive dielectric behaviors and in strong deviations from standard design principles typically employed in the design of dielectric composite systems.

Keywords Dielectric properties · Interfacial effects · Polymer matrix composites · Polymer nanocomposites · Synthetic elastomers · Synthetic rubber · Barium titanate · Graphene oxide · Carbon black · Ceramic nanoparticles · Multi-filler composites · Composites with clustered nanofillers

B. Li
Piezoelectric Technology, PolyK Technologies, LLC, State College, PA 16803, USA

G. Polizos
Electrification and Energy Infrastructure Division, Oak Ridge National Laboratory, Oak Ridge, TN 37831, USA
e-mail: polyzosg@ornl.gov

E. Manias (✉)
Department of Materials Science and Engineering, and Center for Dielectrics and Piezoelectrics, CDP, Materials Research Institute, The Pennsylvania State University, University Park, PA 16802, USA
e-mail: manias@psu.edu

Abbreviations

CB	Carbon black
DRS	Dielectric relaxation spectroscopy
EPDM	Random copolymer from ethylene, propylene, and diene monomers
GO	Graphene oxide
HN	Havriliak–Negami relaxation
MW	Maxwell–Wagner polarization
MWS	Maxwell–Wagner–Sillars polarization
PDMS	Polydimethylsiloxane
ppb	Pixels-per-box (viz. TEM cluster analysis)
rGO	Reduced graphene oxide
SBR	Styrene-butadiene rubber

α, β	Peak shape parameters (e.g., Havriliak–Negami equation)
d_f	Fractal dimension
d_w	Diffusion exponent
D	Diffusion coefficient
e	Electron charge
ε^*	Complex permittivity [function, $\varepsilon^*(\omega, T, \dots)$, with $\varepsilon^* = \varepsilon' - i\varepsilon''$]
ε_0	Vacuum permittivity
ε'	Permittivity, real part of complex permittivity (function, $\varepsilon' \equiv \mathrm{Re}[\varepsilon^*]$)
ε''	Imaginary part of complex permittivity (function, $\varepsilon'' \equiv \mathrm{Im}[\varepsilon^*]$)
$\Delta\varepsilon$	Dielectric relaxation strength [permittivity change between the onset and the end of a relaxation, $\Delta\varepsilon \equiv \varepsilon'(\omega_{\text{onset}}) - \varepsilon'(\omega_{\text{end}})$]
f	Frequency ($f = \omega/2\pi$)
f_{max}	Characteristic frequency of a relaxation (f at ε'' peak maximum/inflection-point)
k_B	Boltzmann's constant
k	Dielectric constant [empirical; typically, the permittivity ε' value at the application relevant frequency range and temperature; often a weak function (of frequency, temperature) rather than a mathematical constant]
ξ	Cluster size
σ	Conductivity (function, can be complex/real/imaginary, σ^*, σ', σ'', *See* permittivity)
s, σ_0	Conductivity parameters (frequency power and amplitude as $\omega \to 0$, e.g., HN equation)
T	Temperature
τ	Relaxation time
$tan\,\delta$	Dissipation factor, loss tangent [function, for dielectric $tan\ \delta(\omega) = \varepsilon''(\omega)\big/\varepsilon'(\omega)$; for mechanical: lossmodulus over storage modulus]
ω	Frequency ($\omega = 2\pi f$)

1 Introduction

Compared to other material classes, such as ceramics, polymers typically possess higher electrical breakdown strengths but lower values of dielectric permittivity. At the same time, materials with high dielectric constants are vital to electrical and electronic applications—such as power systems, electronic equipment, and energy storage devices—and oftentimes flexible geometries are required, or high mechanical strains are expected to occur during the usual operation. In such cases, polymer elastomers are typically the only viable material choice that can combine high mechanical flexibility and toughness with sufficiently high dielectric permittivity. However, elastomeric polymers are typically characterized by relatively low dielectric permittivities, and proper composite design is required to substantially improve the dielectric performance (e.g., increased dielectric permittivity, at low dielectric loss and high breakdown strength), so as to meet application requirements, ranging from simple electrical insulation, to advanced capacitors and high-k dielectrics, to efficient electromagnetic interference shielding. Currently, the predominant approach to obtain elastomer-type materials with such property sets is the addition of high-permittivity inorganic fillers and/or conductive carbon black and graphitic fillers, i.e., through elastomer composites. The design of these multi-component materials relies heavily on established models that predict composite dielectric responses based on the constituents' permittivities, i.e., of the polymer matrix and filler(s): In such design approaches, models (e.g., micromechanical mixing rules, Lichtenecker's logarithmic mixing rule, Maxwell–Wagner equation, Bruggeman model, etc.) are employed for selecting the type and concentration of dielectric fillers in composites, so as to achieve the desired composite properties [1, 2]. However, such models result in increasingly inaccurate estimations of the composite dielectric properties when interfacial effects begin to dominate (e.g., for high aspect-ratio fillers, sub-micron and nanosized particles, multi-filler composites, or whenever extensive polymer/filler interphases with complex nature and an a priori unknown dielectric behavior exist) [1–5]. Furthermore, composites with anisotropic distribution of fillers can also have significant differences in their response compared to conventional composite models, since the dielectric response can vary substantially between different loci in a composite: e.g., composites with aligned or clustered fillers versus composites with random filler dispersions, or multi-filler composites versus single-type filler composites.

Here, we discuss selected examples where synthetic elastomer polymer composites, reinforced by ceramic-dielectric particles and/or carbon-based conductive fillers, exhibit behaviors that depart from the typical dielectric responses. Hence, the science underlying such non-typical behaviors can provide ideas, opportunities, approaches, and paradigms, for elastomer composites with fundamentally new, emergent, or highly improved dielectric responses.

2   Anisotropic Composite Elastomers

Polydimethylsiloxane with Aligned Barium Titanate Nanoparticles
Elastomer composites with anisotropic distribution of the fillers can have significant advantages over conventional composites with random dispersion of the fillers. Filler alignment can be induced using a shear force or by applying an external electric field with high strength. The tailored filler anisotropy can result in marked improvements in energy storage systems, as well as in flexible membranes with enhanced separation or barrier properties [6–13].

Anisotropic composite silicone elastomers based on polydimethylsiloxane (PDMS, Sylgard184®) filled with $BaTiO_3$ (median particle size 190 nm) were synthesized using dielectrophoretic alignment of the fillers [9]. An external electric field (1.6 kV/mm at 100 Hz) was applied to the elastomer/particle suspension during the curing process. The spatial distribution of the aligned fillers in the elastomer matrix is shown in the scanning electron microscopy (SEM) image in Fig. 1. Dielectric relaxation spectroscopy (DRS [14]) was used to measure the dielectric properties
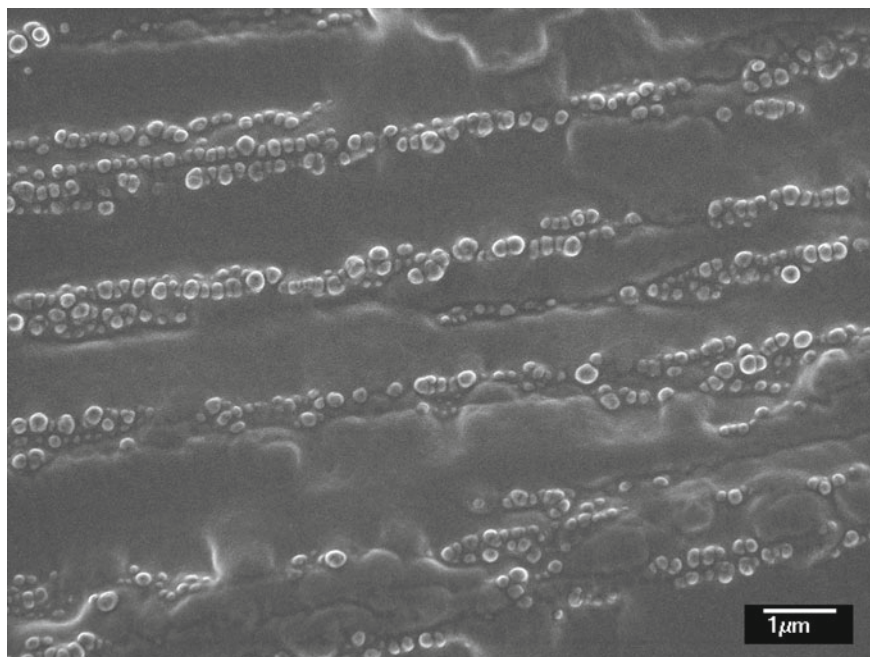

Fig. 1 SEM image of the PDMS elastomer with dielectrophoretically aligned $BaTiO_3$ fillers (10 vol%). Figure reproduced with permission from Ref. [9]. Copyright 2008 Amer. Inst. Physics
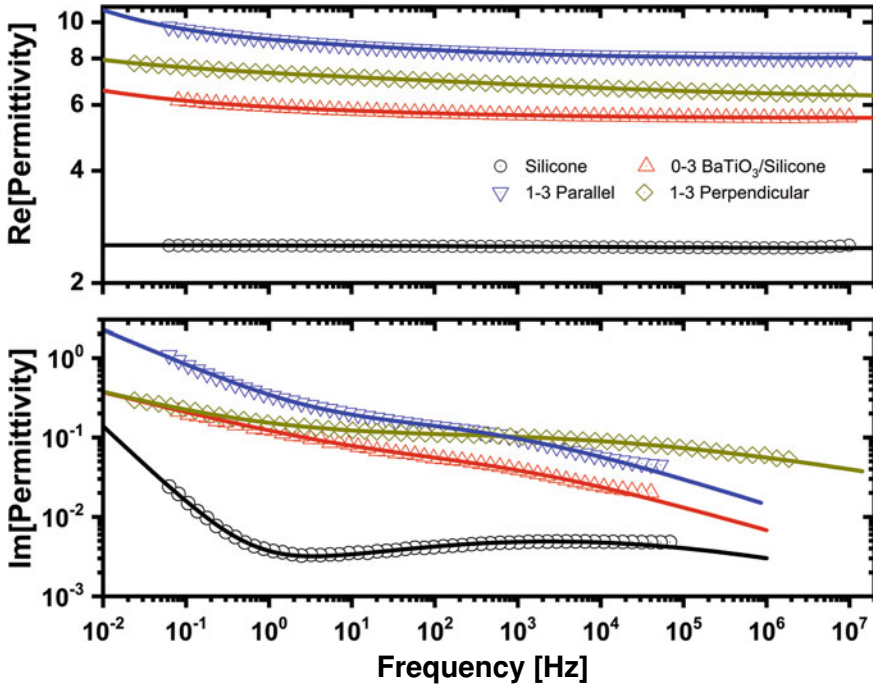
Fig. 2 Real and imaginary parts of the complex permittivity at 293 K (20 °C) of PDMS composites filled with 22.5 vol% BaTiO$_3$. The lines are the best fit of the HN expression and a conductivity power law contribution to the experimental data. Figure reproduced with permission from Ref. [9]. Copyright 2008 Amer. Inst. Physics

of the structured composites at directions parallel (1–3 parallel[1]) and perpendicular (1–3 perpendicular. See Footnote 1) to the direction of the applied field. The pristine silicone elastomer and an elastomer with random filler dispersion (0–3 composite. See Footnote 1) were also measured. The pristine elastomer was subjected to the same thermal cycling under the same external field as the structured elastomers. The real and imaginary parts of the complex permittivity of the elastomers filled with 22.5 vol% BaTiO$_3$ are shown in Fig. 2 Least-square fitting to the experimental data was performed using the Havriliak-Negami (HN) expression and a conductivity contribution [14, 15]:

$$\varepsilon^*(\omega) = \varepsilon_\infty + \frac{\Delta\varepsilon}{\left[1 + (i\omega\tau_0)^{1-\alpha}\right]^\beta} - i\frac{\sigma_0}{\varepsilon_0}\omega^{-s} \tag{1}$$

---

[1] 0–3 stands for a composite with the fillers not being aligned in any direction. 1–3 parallel and 1–3 perpendicular denote composites with the fillers being aligned parallel and perpendicular to the direction of the electric field, respectively.

Table 1 Fitting parameters of Eq. (1) to the experimental data in Fig. 2. Table was adapted with permission from Ref. [9]. Copyright 2008 Amer. Inst. Physics

Sample	α	B	$\Delta\varepsilon$	f_{max} (Hz)
Silicone	0.76 ± 0.01	1	0.05 ± 0.01	2518 ± 641
0–3 BaTiO$_3$/silicone	0.65 ± 0.03	1	0.15 ± 0.02	194 ± 47
1–3 parallel	0.66 ± 0.01	1	0.76 ± 0.01	68 ± 8
1–3 perpendicular	0.78 ± 0.02	0.75 ± 0.08	1.14 ± 0.06	649 ± 143

The values of the shape parameters (α, β), dielectric strength ($\Delta\varepsilon$), and maximum frequency f_{max} of the relaxation mechanism are summarized in Table 1. A weak mechanism process is shown in the dielectric losses of the pristine polydimethylsiloxane elastomer due to interfacial Maxwell–Wagner–Sillars (MWS) polarization effects that are associated with ionic (catalyst, space charge) residues at the interfaces of loci with different crosslinking densities [16]. The dielectric strength of this relaxation mechanism is significantly higher in the elastomer composites and particularly in the structured composites (which possess a preferred filler orientation, parallel or perpendicular to the electric field direction). The increase in the $\Delta\varepsilon$ values originates from the interactions between the elastomer and the high permittivity BaTiO$_3$ fillers. The variation in the values depends on the filler spatial configuration. A shift toward lower frequencies of the f_{max} is observed for the composites due to the slowdown of the dynamics at the elastomer/filler interface. The effect of the filler spatial distribution is also evident in the real part of the permittivity. The $\varepsilon'(\omega)$ values increase substantially in the BaTiO$_3$ composites and the highest values were measured at direction parallel to the filler alignment. The increase of the permittivity due to the filler alignment becomes even more prominent at high electric fields (Fig. 3) and can result in important improvements in the energy storage of capacitors operating at high voltage [9].

3 Styrene-Butadiene Elastomers Filled with Functionalized Graphene Oxide

Styrene-butadiene rubber (SBR) is one of the most widespread and used elastomers with numerous applications. Commercially available reinforced SBR composites are typically based on metal oxides (i.e., silica) or carbon black fillers. The dispersion of metal oxide fillers is thermodynamically favorable when sulfur-based silanes are used during the mechanical mixing and crosslinking of the SBR matrix. The dispersion of carbon black can also be easily accomplished due to the hydrophobic nature of the SBR matrix. Graphene oxide (GO) is a high performance, high surface area carbon filler. Its planar geometry and the strong interaction with the styrene groups of the SBR are ideal for achieving mechanically robust interfaces with the elastomer matrix. Moreover, the oxygen-based functional groups (i.e., C $=$ O, C$-$O, O $=$ C$-$OH) on
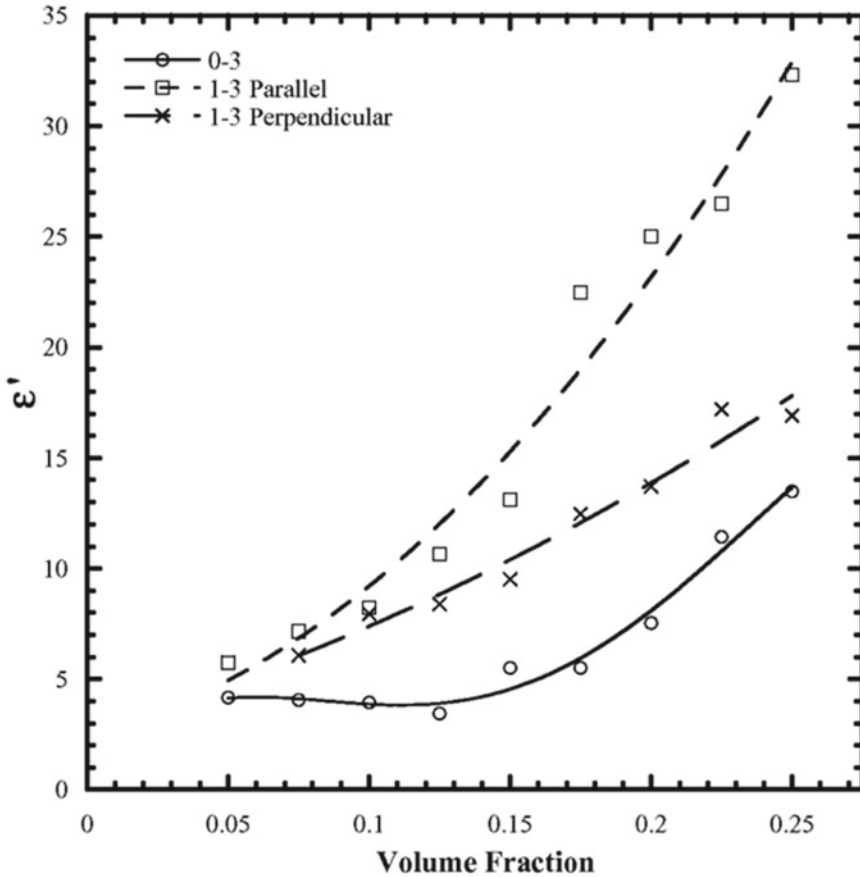
Fig. 3 Permittivity values of the structured composites at different $BaTiO_3$ volume fractions. Figure reproduced with permission from Ref. [9] Copyright 2008 Amer. Inst. Physics

the surface of the GO provide sites that can be functionalized, increase the d-spacing of the GO planes and improve their dispersion.

GO fillers with thiol and dodecylamine (GO–DA) functionalities were synthesized [17]. The thiol-modified GO fillers have reactive interfaces and can be crosslinked with the SBR matrix during the mechanical mixing. During the functionalization process, GO was partially reduced (rGO) and the oxygen content on the surface of the fillers was decreased [18, 19]. The rGO–SH fillers were dispersed in the SBR using a Brabender mixer that was operated at 110 °C. The dodecylamine functionality resulted in a hydrophobic interface on the GO surface and allowed the solution mixing of the GO–DA fillers with the SBR in toluene. The composite matrix was coagulated in methanol and was dried in vacuum at 80 °C. The high-resolution XPS spectra of the GO and the rGO–SH for the C1s and O1s are shown in Fig. 4. The reduction of the GO fillers during the functionalization is clearly shown by the significantly

Table 2 Filler properties: particle size; Filler permittivity ε_r (particle or bulk, the *expected* dielectric ε value of the fillers in the composites); and *measured effective* filler permittivity $\varepsilon_r{}^{effective}$ in composites (filler permittivity as quantified from the EPDM composite permittivity: the $\varepsilon_r{}^{effective}$ combines the filler ε_r plus any interfacial contributions, synergistic or antagonistic). Table adapted with permission from Ref. [32]. Copyright 2021 by the authors (Springer)

Filler[a]	Filler particle size (pm)	Filler	Filler $\varepsilon_r{}^{effectlve}$ in the composite				
		ε_r	20 Hz	60 Hz	140 Hz	1 kHz	10 kHz
SiO_2	1–2	&0 4	42	30	26	21	18
TiO_2	1–2	&0 260	158	138	155	148	142
Sakai-BaTiO$_3$	0.4	&1 3060	537	506	507	495	462
Ionized-BaTi0$_3$	0.4	&1 3420	765	780	787	747	740
Ferro–BaTi O$_3$	(fine) 0.6–0.9	&0 9000	328	375	333	310	302
Ferro-BaTi O$_3$	(coarse) 0.9–1.7	&0 9000	601	605	570	565	550
(Nb, In)TiO$_2$	1–2	&2 60000	141	142	142	130	116

$^{\&0}$Measured by the supplier; $^{\&1}$Measured in suspension; $^{\&2}$Measured at 100 Hz after sintering
[a]The ceramic fillers are: **(i)** *As-received* particulates: SiO$_2$ (S5631, Sigma-Aldrich); Sakai-BaTiO$_3$ (BT-04, Sakai Chemical Industries); Ferro-BaTiO$_3$ (ZL9000, Ferro Electronic Materials, sieved to separate coarse and fine particulates/agglomerates), and TiO$_2$ (Rutile 43047, Alfa Aesar). **(ii)** *Surface-modified* particulates: ionized-BaTiO$_3$ (by washing the Sakai-BaTiO$_3$ with distilled water, stirring overnight, and drying at 80 °C, increasing the mobile ions concentration at the BaTiO$_3$ external surface); and "colossal dielectric permittivity" (Nb + In) co-doped TiO$_2$ (termed as (Nb, In)TiO$_2$, measured to have ε' (100 Hz) = 60,000 after sintering, prepared as per [45])

lower intensity of the C−O peak in the C1s spectra. The surface composition of the C−O groups was 22.3 and 8.6 at % for the GO and rGO–SH fillers, respectively. The composition of the C (sp^2) was 7.9 and 43.3 at % for the GO and rGO–SH fillers, respectively. Similar trends were found for the composition of the O = C−OH groups that was 6.0 and 1.3 at % for the GO and rGO–SH fillers, respectively. TEM images of the non-crosslinked SBR/GO and SBR/rGO–SH composites are shown in Fig. 5. The mechanical properties of the composites were measured using dynamic mechanical analysis (DMA) at 1 Hz over a broad temperature range. The heating rate was 5 K/min. Comparison plots of the storage modulus and tanδ are shown in Fig. 6. The GO and GO-modified filler contents were 4 wt %. The properties of the GO-based composites were compared to the SBR filled with 9 wt% silica nanoparticles (SBR/SnP). Silica is the most frequently used filler material [20, 21].

The comparison with the SBR/SnP was performed to establish performance improvements with respect to baseline composites. All composites were non-crosslinked. The fillers in the SBR/SnP, SBR/GO, and SBR/rGO–SH composites were dispersed by mechanical mixing. The SBR/GO and SBR/rGO–SH composites have comparable modulus values. In the glassy state (T < −40 °C), their modulus plateau values are 44% higher than that of the SBR/SnP even though their filler weight content is less than half compared to that of the silica composite. The higher performance of the GO fillers can be associated with their higher surface area and planar geometry that resulted in improved interfacial adhesion with the SBR matrix.
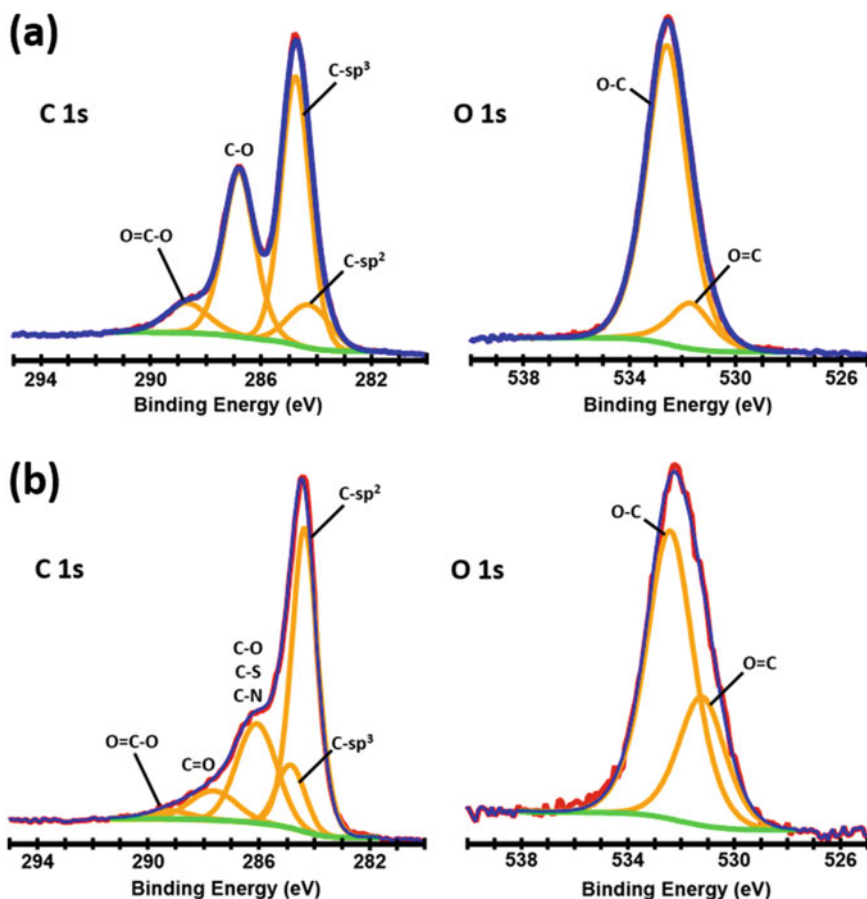
Fig. 4 High-resolution XPS spectra of the **a** GO and **b** rGO–SH. Figure reproduced from Ref. [17]. Copyright 2020 by the authors (CC attribution license)

The GO–DA fillers were dispersed in the SBR using solution mixing. The mixing was promoted by the hydrophobic functionality of the GO–DA fillers and the SBR/GO–DA composite showed more notable improvements. The storage modulus increased by 60 % in the glassy state and the rubbery plateau values at high temperatures (T > 20 °C) increased almost 200%. The tanδ values in Fig. 6b show a peak at −32 °C that is associated with the glass transition temperature of the elastomer matrix. The shoulder at higher temperatures is attributed to an interfacial relaxation mechanism with slower dynamics due to an interfacial SBR phase that is adsorbed on the surface of the fillers [22]. This interfacial mechanism is more pronounced in the SBR/GO–DA composite due to the better filler–elastomer interfacial adhesion. The peak intensity (and area) of the tanδ peak is also significantly lower for the SBR/GO–DA
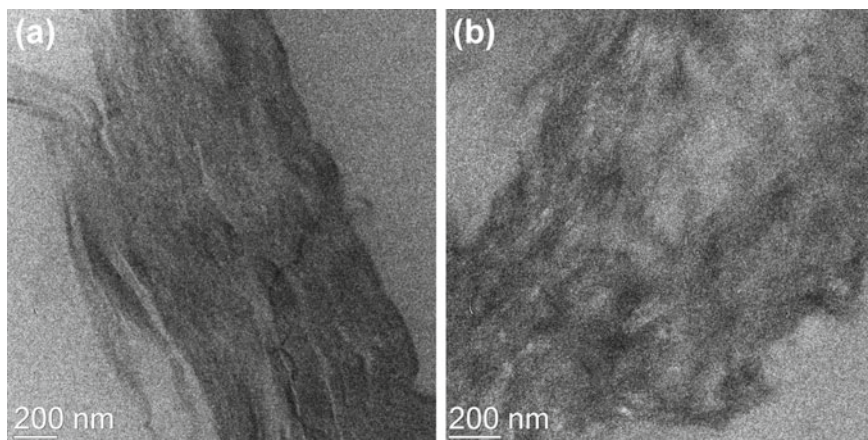
Fig. 5 TEM images of the **a** SBR/GO and **b** SBR/rGO–SH. Figure reproduced from Ref. [17]. Copyright 2020 by the authors (CC attribution license)
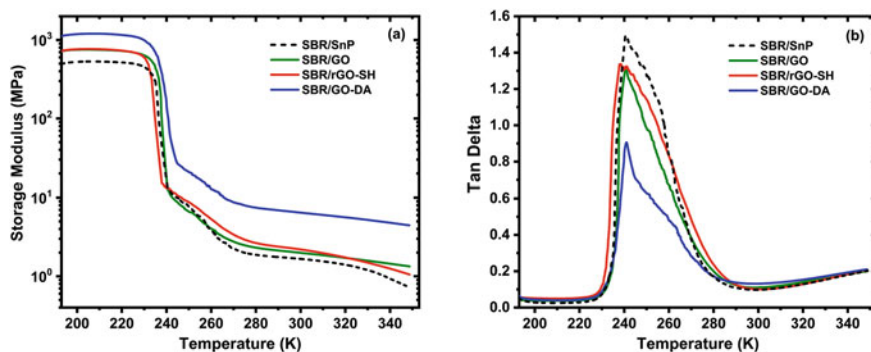

Fig. 6 Comparison plots of the mechanical properties of the SBR composites according to DMA measurements. **a** storage modulus and **b** tanδ. Figure reproduced from Ref. [17]. Copyright 2020 by the authors (CC attribution license)

composite due to less mobile SBR/GO–DA interface. Tailoring the interfacial chemistry of the GO fillers can make their mixing with hydrophobic elastomer matrices thermodynamically favorable and result in highly reinforced elastomer composites.

4 Elastomer Composites with Clustered Nanoparticulate Fillers

EPDM Elastomer Composites with Conductive Carbon Black

For many applications, the increased permittivity in high-k ceramic polymer composites cannot meet the desired requirements. Conductive fillers are therefore employed, as they can offer a dramatic increase in dielectric permittivity near percolation transition (ε' up to 10^3–10^4) [23], when appropriate measures are taken to reduce or prevent percolative electrical conduction. Such composites have attracted considerable attention for applications as dielectrics, including charge storage capacitors, high-k gate dielectrics, electromagnetic interference shielding, electroactive materials [24–28].

Typically, it is assumed that the substantial increase in dielectric permittivity is associated with the formation of microcapacitor networks, within which charge carriers can migrate too and accumulate at the filler–polymer interfaces (essentially an interfacial polarization, typically modeled as Maxwell–Wagner–Sillars relaxation [14, 23, 30, 31]). Despite the success of this approach in quantifying the behavior of multiple materials, there are many instances where there exit discrepancies [32]. Here, we review a recent study of a near-percolated polymer composite, based on an ethylene propylene diene polymer (EPDM, Vistalon 5420, ExxonMobil Chemical) with 32 wt% carbon black (CB, Spheron 6000, Cabot [33]). These nanocomposite materials deviate in dielectric response from the behavior expected under the usual assumptions of microcapacitor networks (*vide infra*).

Figure 7a shows representative TEM images of the composite structure. Individual CB particles with an average size of 100 nm are clustered into CB aggregates, which are well distributed across the entire composite sample. CB particles in the aggregates are strongly connected by nanometer-thin immobilized bound polymer layers [34], and the arrangement of CB can be described by a fractal dimension (d_f) [35, 36]:
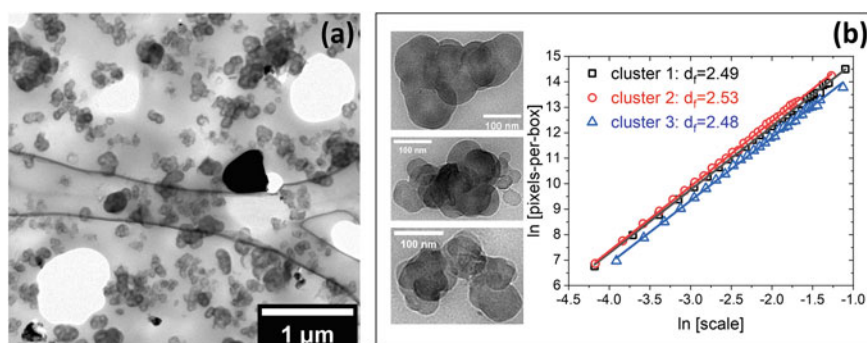

Fig. 7 **a** TEM image of CB polymer composite. The larger dark-colored particles are a second type of ceramic fillers. **b** Derivation of the fractal dimension for the clusters using the pixel-counting algorithm: TEM images of three CB clusters and the corresponding analyses. Figure and data adapted with permission from Ref. [29]. Copyright 2021 by the authors

$$N(r) \sim r^{d_f} \tag{2}$$

where r is the size of the cluster containing $N(r)$ number of CB particles. For the EPDM/CB composites in question, the fractal dimension of the CB clusters could not be directly measured by SAXS, due to the low angle limit of our instruments, and instead, we used the fractal box method (pixel-counting algorithm) to estimate its value [37, 38]. Specifically, grids with varying numbers of boxes are overlaid on a TEM image containing each CB cluster, and the average number of pixels in each box is counted as pixels-per-box (ppb). The fractal dimension of this CB cluster can be calculated from the pixel-counting plot (i.e., ln(ppb) vs. ln(box size)), as shown in Fig. 7b, and as expected different CB clusters in the same composite show a very similar fractal dimension, namely $d_f \cong 2.5$.

For these EPDM/CB composites, Fig. 8 provides the temperature- and frequency-dependent dielectric properties. At each temperature, a strong dielectric relaxation can be identified, manifested by a strong step change in dielectric permittivity and an associated peak in ε''. To better understand the polarization mechanism, the dielectric
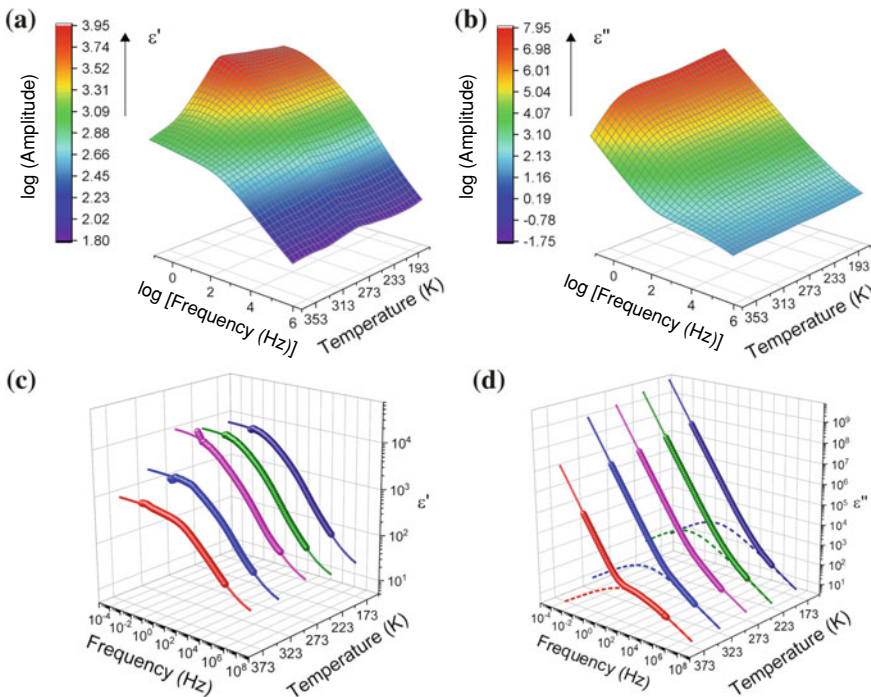

Fig. 8 **a**, **b** Dielectric spectra of a near-percolated EPDM/CB composite as a function of temperature and frequency, as well as **c**, **d** the best fitting Cole–Cole curves. Figure and data adapted with permission from Ref. [29]. Copyright 2021 by the authors

spectra of the polymer composite are analyzed within the framework of the Cole–Cole equation plus a conductivity contribution (Eq. 1 with β and s values set equal to 1.0, for a detailed discussion on the choice of fitting equation, we refer to [39]). The fitting curves are also shown in Fig. 7, indicating a good fitting of the experimental data to the Cole–Cole model.

The results from the best fit are plotted in Fig. 9a–d. Interestingly, the evolution of polarization does not follow the trends as generally expected from MWS polarization. Specifically, as shown in Fig. 9a, b, the relaxation strength and relaxation time increase with temperature in the lower-temperature region, whereas in the higher temperature region, both parameters decrease with temperature. This non-monotonic temperature evolution indicates a rather complex nature for the dielectric relaxation in the polymer composite, which cannot be described by a simple thermal activation model. The same is also observed in Fig. 9c, where the conductivity keeps decreasing with increasing temperature, again manifesting a departure from simple thermally activated mechanism. The shape parameter demonstrates a nearly constant value of 0.6 (Fig. 9d), and in fact, this value provides strong evidence for the relevant mechanism (*vide infra*, Eq. 7).
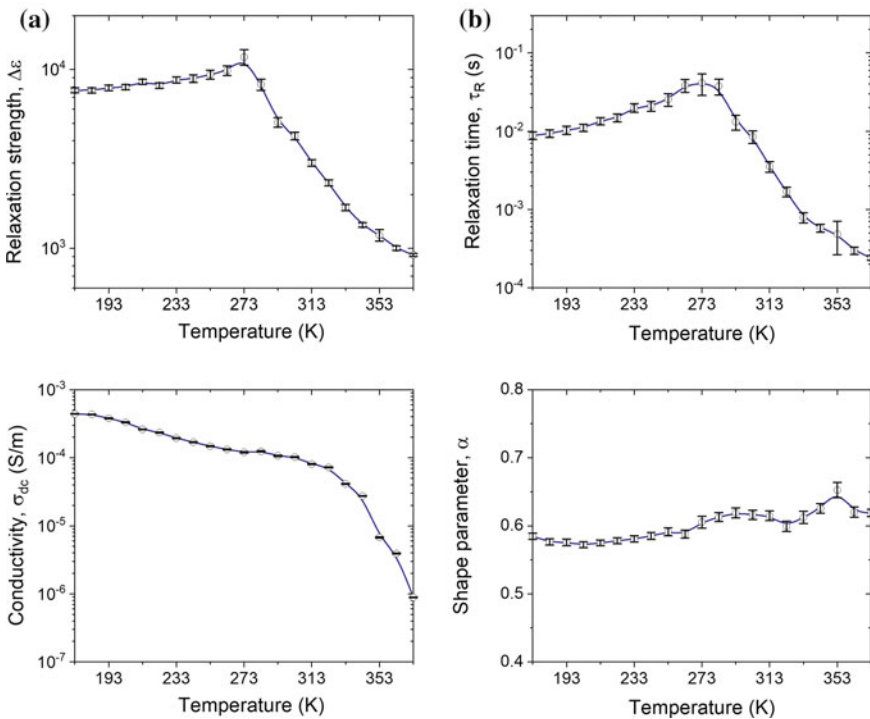

Fig. 9 Best-fit parameter values for the Cole–Cole model at different temperatures. Figure and data adapted with permission from Ref. [29]. Copyright 2021 by the authors

The evolution of the various dielectric variables indicates the significance of the morphology of the CB filler clusters, as defined through electrical connectivity, rather than simple topological/geometric definition. Reducing temperature evidently corresponds to better electrical connectivity between the CB particles within the cluster, which would be equivalent to shrinkage of the EPDM matrix and closer proximity of the CB particles, or also equivalent to increasing filler concentration, accounting for the increased conductivity with reducing temperature. Along the same lines, the T-dependence of relaxation strength and relaxation time is strongly reminiscent to the divergence of filler cluster size typically observed across the percolation threshold [36, 40], as long as both parameters are positively correlated with cluster size. From this perspective, the measured dielectric and electrical responses can be quantified by considering the electron transport along the electrically connected CB fillers (within clusters or across networks), and one can provide scaling relations between the various dielectric variables and the CB cluster morphology.

For these EPDM/CB polymer composites, since the CB network is self-similar over different length scales (fractal nature), one can define (Eq. 3) the fractal dimension (d_f) of the CB aggregates at different length scales, as

$$N(r) \sim r^{d_f} \quad \text{where} \quad \begin{cases} d_f = 2.5, \ r < \xi \\ d_f = 3, \quad r > \xi \end{cases} \tag{3}$$

r is the size of a CB aggregate containing $N(r)$ number of CB particles (similar to Eq. 2). Within a CB cluster (of size ξ), the fractal dimension (d_f) of CB arrangement is 2.5, whereas macroscopically, beyond the single-cluster size ($r > \xi$), the CB fillers can be regarded as a homogenous three-dimensional dispersion with $d_f = 3$ [36, 41, 42]. Such a fractal CB particle arrangement, would result in electron transport that scales accordingly over the same length scales, i.e., with the mean square displacement of electrons $< r^2(t) >$ scaling with time (t) as [35, 36])

$$< r^2(t) > \sim t^{2/d_w} \quad \text{where} \quad \begin{cases} d_w = 3.8, \ r < \xi \\ d_w = 2, \quad r > \xi \end{cases} \tag{4}$$

That is, electron transport within one CB cluster follows an "anomalous diffusion" with a diffusion exponent $d_w = 3.8$, whereas electrons travel between clusters is governed by normal (charges in external electric field, or even Fickian) diffusion $< r^2(t) > \sim t$.

5 Frequency Dependence of Dielectric Properties

For the frequency dependence of dielectric properties, one can first consider the frequency-dependent AC conductivity: At each temperature, the conductivity ($\sigma(w)$) is proportional to the number density of electrons participating in the conduction

process (n) and the diffusion coefficient (D) via $\sigma(w) \sim nD$. The number density of conduction electrons (n) is proportional to the solid concentration of CB in a blob (as defined by a collection of CB particles in electrical contact to each other, i.e., a collection of CB particles that the electrons can explore during one period of measurement, t). This blob size (r) can be estimated from Eq. (4) as $r \sim t^{1/d_w}$ and using Eq. (3), one can get

$$n \sim \frac{N(r)}{r^3} \sim r^{d_f-3} \sim t^{(d_f-3)/d_w} \tag{5}$$

The diffusion coefficient (D) will simply be the mean square displacement of the electrons over the same period of measurement (t), and thus Eq. (4), yields

$$D \sim \frac{\langle r^2(t) \rangle}{t} \sim t^{(2-d_w)/d_w} \tag{6}$$

and combing Eqs. (5) and (6), would result in the frequency dependence of conductivity:

$$\sigma(w) \sim nD \sim t^{(d_f-d_w-1)/d_w} \sim w^{(d_w-d_f+1)/d_w} \sim \begin{cases} w^{0.605}, r < \xi \\ w^0, r > \xi \end{cases} \tag{7}$$

The conductivity of the polymer composite will exhibit different power law dependences on frequency, when electrons explore a single cluster versus when they explore larger length scales. The crossover frequency corresponds to the critical time scale when electrons can explore one entire cluster, and identifies the transition from anomalous diffusion to normal diffusion for electron transport.

It is interesting to note that the scaling exponent of the high-frequency conductivity (0.605), is very close to the shape parameter (α) measured from the experimental data (Fig. 9d). As defined in Eq. (1), α characterizes the slope of the loss (ε'') curve of dielectric relaxation and should have the same value as the slope of conductivity (σ_w) at the high-frequency end, as $\sigma_w = 2\pi f \varepsilon_0 \varepsilon''$. A consistent α value of ~0.6 measured across the whole temperature range confirms our assumption of electron displacement as the dominant relaxation mechanism in the CB polymer composite.

6 Cluster Size Dependence of Dielectric Properties

In order to confirm the validity of the above scaling relations, one can use these scaling relations to determine the cluster size dependence of the various dielectric variables measured by dielectric spectroscopy. Thus, by using the TEM-determined cluster size and fractal dimension and the DRS-determined dielectric quantities, one can directly compare the scaling laws versus the experimental trends. The dielectric variables that

can be investigated are the DC conductivity (σ_{dc}), the relaxation strength ($\Delta\varepsilon$), and the relaxation time (τ_R), as quantified by the fitted parameter values of the Cole–Cole function.

7   Scaling of Conductivity (σ_{dc}) with Custer Size

At low-frequency limit, the DC conduction (σ_{dc}) can be calculated by

$$\sigma_{dc} = \frac{e^2 n}{k_B T} D \tag{8}$$

where e denotes the electron charge; n and D are the number density of conduction electrons and the diffusion coefficient, respectively, as defined before; k_B and T are the Boltzmann's constant and temperature, respectively [35, 41, 43]. For long-range electron transport, n and D are independent of time, but they are strong functions of cluster size (ξ), since the number density of conduction electrons is proportional to the solid concentration of CB in the cluster, that is

$$n \sim \frac{N(\xi)}{\xi^3} \sim \xi^{d_f - 3} \tag{9}$$

and from the definition of $N(\xi)$ and ξ, for a CB cluster was experimentally determined to be $d_f \cong 2.5$.

The diffusion coefficient can be calculated by simply considering that the electrons explore the cluster size ξ, i.e., a mean square displacement of ξ^2, over a time interval t_ξ (as described in Eq. 4, with $t_\xi \sim \xi^{d_w}$ and $d_w = 3.8$, as it applies to electron transport within a cluster):

$$D \sim \frac{\xi^2}{t_\xi} \sim \xi^{2 - d_w} \tag{10}$$

combining Eqs. (9) and (10) with Eq. (8), the DC conductivity and cluster size ξ, scale as

$$\sigma_{dc} = \frac{e^2 n}{k_B T} D \sim \frac{n D}{T} \sim \frac{\xi^{d_f - d_w - 1}}{T} = \frac{\xi^{-2.3}}{T} \tag{11}$$

8 Scaling of Relaxation Time (τ_R) and Relaxation Strength ($\Delta\varepsilon$) with Cluster Size

The polarization of the conductive CB filler clusters originates from the electron transport within a cluster (over longer time scales, electrons can travel beyond the cluster, follow normal diffusion, result in a DC conductivity, and do not contribute to the polarization). Consequently, the relaxation time measured from the dielectric spectrum (τ_R) should scale with the time needed for electrons to explore a cluster (t_ξ, as defined in Eq. 4).

$$\tau_R \sim t_\xi \sim \xi^{d_w} = \xi^{3.8} \tag{12}$$

The dielectric relaxation strength that corresponds to the conductive filler cluster polarization, can be considered as the relaxation of a number of individual dipoles with a total dipole moment (P), for which [44]:

$$\Delta\varepsilon = \frac{NP^2}{3\varepsilon_0 k_B T} \tag{13}$$

where N is the number density of dipoles; ε_0 is the vacuum permittivity; k_B and T are the Boltzmann's constant and temperature, respectively. In analogy, for the EPDM/CB polymer composites, we can have

$$\Delta\varepsilon = \frac{NP^2}{3\varepsilon_0 k_B T} \sim \frac{Nq^2\xi^2}{T} \tag{14}$$

with N now being the number density of clusters; P being the equivalent dipole moment of polarized clusters, which is proportional to the number density of electrons in the cluster (q) and the cluster size (ξ). Since the electron density in a cluster (q) also scales with the concentration of CB in the cluster, i.e., $N(\xi)/\xi^3 \sim \xi^{d_f-3}$ (Eq. 9): Nq should be proportional to the CB concentration in the composite and, therefore, is a constant in this case. Thus, the relaxation strength can be rewritten as

$$\Delta\varepsilon \sim \frac{q\xi^2}{T} \sim \frac{\xi^{d_f-1}}{T} = \frac{\xi^{1.5}}{T} \tag{15}$$

Equations (11), (12), and (15) provide the dependences of measured/fitted dielectric parameters on the cluster size (ξ), which can be replaced (through Eq. 12) by its scaling with the relaxation time (τ_R). In this way, by using the scaling between ξ and τ_R, we can rewrite the scaling relations Eqs. (11), (12), and (15), as dependencies on the relaxation time, rather than on the cluster size:

$$\Delta\varepsilon \cdot T \sim \tau_R^{0.40}; \; \sigma_{dc} \cdot T \sim \tau_R^{-0.61}; \; \sigma_{dc} \cdot T \sim (\Delta\varepsilon \cdot T)^{-1.53} \tag{16}$$
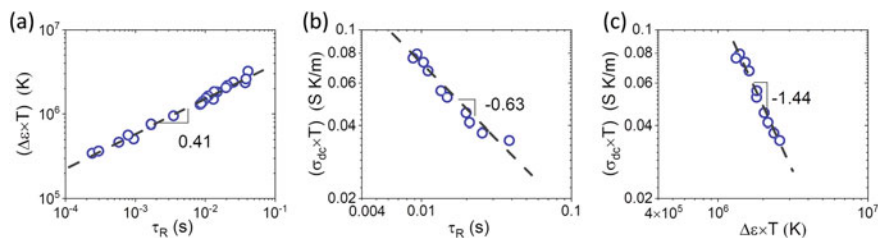
Fig. 10 Scaling relations between various dielectric parameters. The number on the graphs represents the slope of the linear regression on experimental data, which is in good agreement with the scaling prediction. Figure and data adapted with permission from Ref. [29]. Copyright 2021 by the authors

In this way, the derived scaling relations are expressed through only measured/fitted values, and one can use experimental data only, as plotted in Fig. 10a–c, to test the validity of the scaling relations. A good agreement is achieved—maybe surprisingly given some of the simplifications outlined above—but the scaling of the experimental data clearly confirm the scaling relations of the model, making a strong case that the electron transport within the CB clusters is in fact the dominant polarization mechanism.

Finally, since $\Delta\varepsilon$, τ_R, σ_{dc} and α are the fitted variables in HN or in Cole–Cole, once these parameters are experimentally determined, it is possible to quantify the details of the composite/filler morphology and of the filler cluster size based on dielectric data (as illustrated in Scheme 1).

9   Dielectric Response of Multi-filler Elastomer Composites

EPDM Elastomer Composites with Carbon Black and Ceramic Nanoparticles
In order to identify and highlight the interfacial contributions to the composites' dielectric properties, we present some results from elastomer/carbon black/ceramic composites[2]: In these multi-filler composite materials, we added a series of micron-sized ceramic fillers to the EPDM/CB composites discussed in the previous section.

In order to distinguish the relative contributions of the fillers and of the filler interfaces to the macroscopic composite permittivity, a series of ceramic particulates—that span orders of magnitude in permittivity values and have varied surface chemistries—were compared [32]. Specifically, a series of low-loss ceramic fillers were used, with 0.4–2 μm in size, differing in nature (i.e., dielectric/paraelectric SiO_2 and TiO_2 versus ferroelectric $BaTiO_3$), and spanning a wide range of dielectric permittivities (particulate or bulk ε', ranging from 4 to 60,000). For each filler, a series of EPDM composites was prepared, varying the ceramic filler loading from

---

[2] The text and figures of this section were adapted with permission from a conference proceedings paper published in Ref. [32], Copyright 2021 by the authors (B. Li, E. Manias, et al., MRS Advances, Springer).
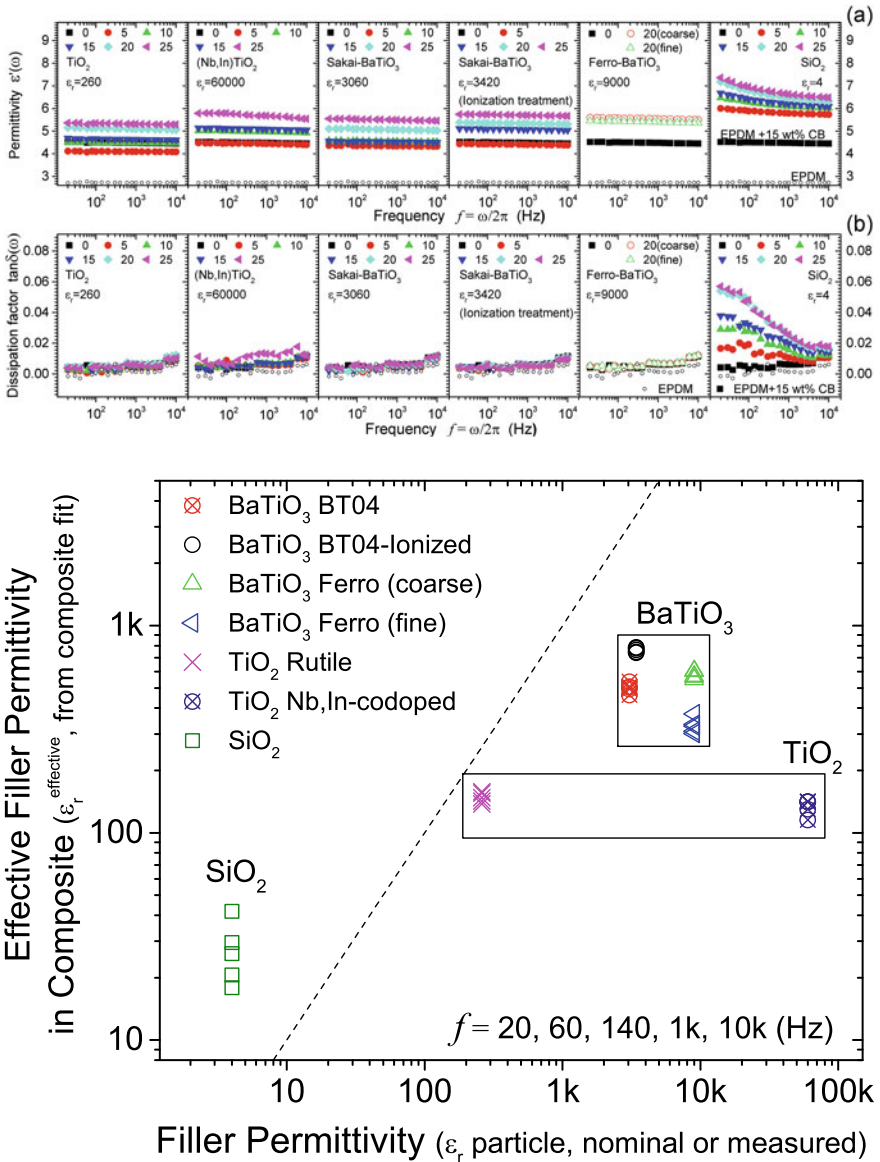
Scheme 1 Schematic illustrating the correlation between dielectric/electrical properties and the carbon black filler-network morphology. Figure and data adapted with permission from Ref. [29]. Copyright 2021 by the authors

5 to 25 wt%, while keeping the carbon black (CB) content constant at 15 wt% and the organic/elastomer matrix the same, i.e., all elastomers had constant monomer: plasticizer and monomer:curing agent ratios (30 phr and 5 phr, respectively). The dielectric properties of the composites were measured as a function of frequency (20– 10 kHz), at 1 V, using a charge–voltage converter (GADD, integrated with a Stanford Research SR830 lock-in amplifier [32]) on rectangular specimens (4 × 1 cm wide, by 3 mm thickness) coated by colloidal silver electrodes, Results were collected by measuring the real part of permittivity, $\varepsilon'(\omega)$, Fig. 11a, and the "dissipation factor", $\tan\delta(\omega)$, Fig. 11b, as per [45].

In a first approach, keeping the carbon black (CB) content constant at 15 wt% across all systems, allows for simplifying the comparative discussion across the various ceramic fillers, by considering the matrix to be the combination of all organics (EPDM, plasticizer, and crosslinker) *plus* the carbon black [1]. In this case, the composite dielectric permittivity, ε, can be quantified by Lichtenecker's logarithmic mixing rule applied to the permittivity of the "matrix" and the ceramic fillers:

$$log\varepsilon = v_f log\varepsilon_r + \left(1 - v_f\right)log\varepsilon_m \qquad (17)$$

Fig. 11 a Dielectric permittivity, $\varepsilon'(\omega)$ and **b** dielectric dissipation factor, tan $delta(\omega)$, as a function of frequency (ω) at room temperature, for EPDM composites (with 0–25 wt% ceramic fillers). **c** The filler's effective dielectric permittivity in the composites (including interfacial contributions, as determined by ε in Lichtenecker's mixing rule) is compared against the particle/filler permittivity ε_r Fittings at five frequencies provide five values for each filler's effective ε (see Table 2). The dashed-line corresponds to a 1:1 relation, i.e., no interfacial contributions. Figure and data adapted with permission from Ref. [32]. Copyright 2021 by the authors (Springer)
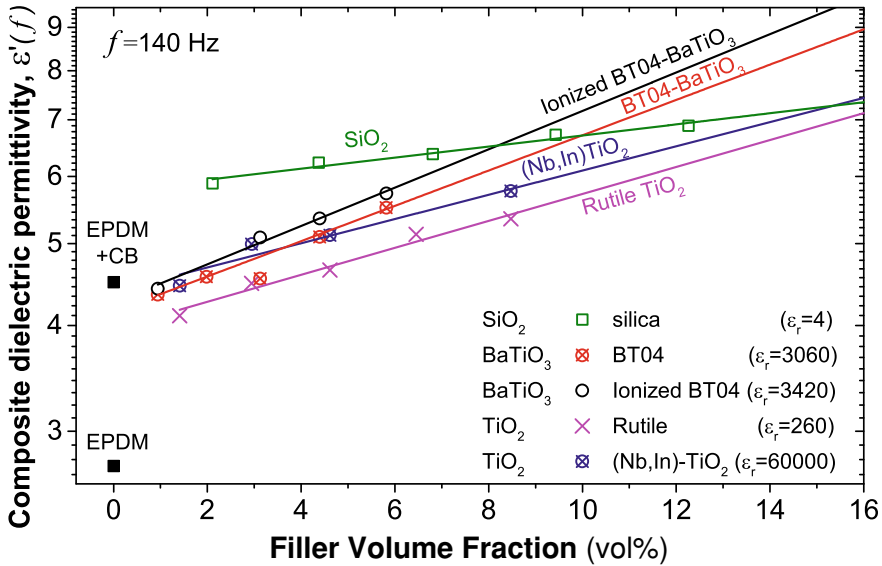
Fig. 12 **a** Measured composite permittivity at 140 Hz and fittings of the permittivities versus filler loading by Lichtenecker's logarithmic mixing rule. Figure and data adapted with permission from Ref. [32]. Copyright 2021 by the authors (Springer)

with ε_r and ε_m being the permittivities of the ceramic filler and the matrix, respectively, and v_f the volume fraction of the ceramic filler (Fig. 12). Subsequent measurement of the macroscopic composite permittivity (ε) as a function of ceramic filler loading (v_f), can thus yield an "effective dielectric permittivity" (ε_r) for each ceramic filler in the composite; i.e., a permittivity value that quantifies the *combined ceramic filler particle plus their interfacial contributions* to the measured composite permittivity (Table 2, Fig. 11c).

10 Effect of the Interphases on the Dielectric Properties of the Composites

The values of $\varepsilon_r^{effective}$ provide a measure of each filler's realistic contribution to the measured composite permittivity, and are found to be markedly different from the values expected (e.g., markedly different from the usual filler "dielectric constants" ε_r used in design considerations, or those used for the mixing rule above: which typically are bulk permittivity values, or particle permittivity values, often averaged over the application relevant frequency and temperature ranges, or measured particle-ε' values). This is a clear indication that the dielectric contributions from the interphases and the interfaces dominate the overall composite permittivity, rather than the ceramic fillers' ε_r dielectric values. Although addition of ceramic fillers does

increase the permittivity of the composites (compared to the unfilled EPDM elastomer, Fig. 12), this increase is qualitatively and quantitatively different from what is expected.

Intuition and typical design models (e.g., mixing rules) predict a larger dielectric permittivity composite, when fillers with higher ε_r are incorporated. However, in Fig. 12, the silica composites exhibit the greatest permittivity (ε-value) among all the composites, despite SiO_2 being the lowest ε_r filler used, when comparing the various ceramic particulates. Also, the composites with the Sakai-BaTiO$_3$ ($\varepsilon_r = 3060$) fillers show higher permittivity values than the composites with Nb + In co-doped TiO$_2$ ($\varepsilon_r = 60{,}000$) fillers. These marked deviations of the measured composite permittivities from the natural expectation that "higher-k fillers should yield higher permittivity composites" [1], strongly indicate that the composite permittivities are dominated by interfacial contributions, which are not considered by most mixing rules [1, 2, 46]. Silica displays, maybe, the most straightforward interfacial behavior: A low-frequency relaxation process can be clearly identified in the EPDM/CB/SiO$_2$ composites (manifested both as a step in the permittivity and an associated peak in the loss, Fig. 11). This is a typical behavior of macroscopic-scale/domain polarization—i.e., Maxwell–Wagner-Sillars (MWS) polarization—arising from the low-frequency sub-diffusive transport of the charge carriers (e.g., ions, surfactants, impurities) within interphases or other domain boundaries, which manifests as an additional increase in permittivity.

For the other fillers, interfacial effects also exist but, rather than a MWS polarization, they seem to influence the composite dielectric performance in a qualitatively different manner: As seen in Fig. 11, there exist no pronounced peaks in tan δ as would be expected from a high-strength MWS mechanism; instead the composite permittivity is almost frequency-independent. Also, in contrast to any common expectation, at low contents (at low ceramic volume fractions 1–2 vol%) the composites exhibit permittivity values lower than the EPDM + CB elastomer: Such composite permittivities, with values below the "matrix" (EPDM + CB) permittivity, cannot be explained by any weighted mixing of matrix and filler permittivities (as it would necessitate a negative filler ε_r value for the ceramics); rather, this behavior reflects contributions from the ceramic particle interphases that are antagonistic to the EPDM/CB dielectric response (e.g., local field effects, restricted mobility for filler-sorbed polymer chains, etc., yielding a reduced permittivity in the interphases compared to the matrix [32, 46]). One way to quantify these interfacial effects, within the Lichtenecker's approximation, would be to use an "effective permittivity" value for each filler (Fig. 12), which combines both filler and interfacial contributions, toward a value that can be substantially different than the filler's permittivity (Table 2). In Fig. 11c, when these "effective permittivities" [of the fillers + interphases in the composites] are compared against the expected values from the filler "dielectric constants", an interesting trend is observed: Fillers are clustered in groups of same filler type (enclosed in boxes in Fig. 11c), where the fillers' dielectric contribution to the composites' permittivity is measured to relate more to the filler type (e.g., same filler chemistry and, consequently, similar interphase characteristics), rather than to each filler's permittivity value. This is completely different to the expected behavior, e.g., mixing rules,

where the fillers' dielectric contribution to the composites ε is expected to relate directly to the permittivity ε_r of the filler particles. For instance, the $\varepsilon_r^{effective}$ of the rutile TiO_2 is nearly identical to that of the Nb, In-doped TiO_2, even though the two fillers differ in permittivity by two orders of magnitude ($230 \times$ difference in ε_r); also, all four different $BaTiO_3$ fillers show similar contributions in the composites (similar values of $\varepsilon_r^{effective}$), despite large variations in their filler/particle dielectric permittivities ε_r (Table 2).

The above comparisons clearly demonstrate that the fillers' effective permittivity and, therefore, how much each filler realistically contributes to the macroscopically observed composite's permittivity, are largely dominated by the interphases and the interfaces, i.e., the nature of the filler (e.g., chemistry, surface characteristics and modifications, etc.), rather than by the filler's permittivity. This conclusion is further manifested in: **(i)** the measurable differences recorded in the fillers' $\varepsilon_r^{effective}$ when considering fillers that only differ in size (e.g., for the Ferro $BaTiO_3$ fillers, the coarse particles have a higher $\varepsilon_r^{effective}$ than the fine identical-type particles, due to lower volume-fractions of the unfavorable interfaces). **(ii)** when comparing fillers that vary only in surface treatment (e.g., the ionized $BaTiO_3$ demonstrates the highest effective permittivity among all other $BaTiO_3$ fillers, because of the extra mobile ions introduced on the filler surfaces, which provide higher space-charge polarization within the interface); and **(iii)** the counter-intuitive antagonistic interphasial response of the ceramics to the carbon black dielectric response (as evidenced by the measured reduction in permittivity upon addition of low concentrations of ceramics to EPDM + CB, Fig. 12), where the ceramic fillers and their interphases limit the carbon black cluster polarization, e.g., by interrupting the CB connectivity (electron tunneling) when ceramic particles are located between adjacent carbon black particles.

Conflict of Interest Declaration The authors declare no conflicts of interest.

References

1. Sihvola AH (1999) Electromagnetic mixing formulas, applications. I.E.T. Books, London, UK

2. Dang ZM, Yuan JK, Zha JW, Zhou T, Li ST, Hu GH (2012) Fundamentals, processes and applications of high-permittivity polymer-matrix composites. Prog Mater Sci 57:660–723

3. Barber P, Balasubramanian S, Anguchamy Y, Gong S, Wibowo A, Gao H, Ploehn HJ, Zur Loye HC (2009) Polymer composite and nanocomposite dielectric materials for pulse power energy storage. Materials 2:1697–1733

4. Smith RC, Liang C, Landry M, Nelson JK, Schadler LS (2008) The mechanisms leading to the useful electrical properties of polymer nanodielectrics. IEEE Trans Dielectrics Electr Insulation 15:187–196

5. Lewis TJ (2005) Interfaces nanometric dielectrics. J Phys D: Appl Phys 38:202–212

6. Li B, Xidas PI, Manias E (2018) High breakdown strength polymer nanocomposites based on the synergy of nanofiller orientation and crystal orientation for insulation and dielectric applications. ACS Appl Nano Mater 1:3520–3530

7. Li B, Xidas PI, Triantafyllidis KS, Manias E (2017) Effect of crystal orientation and nanofiller alignment on dielectric breakdown of polyethylene/montmorillonite nanocomposites. Appl Phys Lett 111:082906

8. Tomer V, Polizos G, Randall CA, Manias E (2011) Polyethylene nanocomposite dielectrics: implications of nanofiller orientation on high field properties and energy storage. J Appl Phys 109:074113

9. Tomer V, Randall CA, Polizos G, Kostelnick J, Manias E (2008) High- and low-field dielectric characteristics of dielectrophoretically aligned ceramic/polymer nanocomposites. J Appl Phys 103:034115

10. Wan J, Xie J, Kong X, Liu Z, Liu K, Shi F, Pei A, Chen H, Chen W, Chen J, Zhang X, Zong L, Wang J, Chen LQ, Qin J, Cui Y (2019) Ultrathin, flexible, solid polymer composite electrolyte enabled with aligned nanoporous host for lithium batteries. Nat Nanotechnol 14:705−711

11. Wang X, Zhai H, Qie B, Cheng Q, Li A, Borovilas J, Xu B, Shi C, Jin T, Liao X, Li Y, He X, Du S, Fu Y, Dontigny M, Zaghib K, Yang Y (2019) Rechargeable solid-state lithium metal batteries with vertically aligned ceramic nanoparticle/polymer composite electrolyte. Nano Energy 60:205−212

12. Zhai H, Xu P, Ning M, Cheng Q, Mandal J, Yang Y (2017) A flexible solid composite electrolyte with vertically aligned and connected ion-conducting nanoparticles for lithium batteries. Nano Lett 17:3182−3187

13. Gao Y, Picot OT, Tu W, Bilotti E, Peijs T (2018) Multilayer coextrusion of graphene polymer nanocomposites with enhanced structural organization and properties. J Appl Polym Sci 135:46041

14. Kremer F, Schönhals A (2003) Broadband dielectric spectroscopy. Springer, Berlin, Heidelberg

15. Havriliak S, Negami S (1966) A complex plane analysis of α-dispersions in some polymer systems. J Polym Sci Polym Symp 14:99−117

16. Fragiadakis D, Pissis P (2007) Glass transition and segmental dynamics in poly(dimethylsiloxane)/silica nanocomposites studied by various techniques. J Non-Cryst Solids 353:4344−4352

17. Park J, Sharma J, Monaghan KW, Meyer III HM, Cullen DA, Rossy AM, Keum JK, Wood III DL, Polizos G (2020) Styrene-based elastomer composites with functionalized graphene oxide and silica nanofiber fillers: mechanical and thermal conductivity properties. Nanomaterials 10:1682

18. Kang SM, Park S, Kim D, Park SY, Ruoff RS, Lee H (2011) Simultaneous reduction and surface functionalization of graphene oxide by mussel-inspired chemistry. Adv Funct Mater 21:108−112

19. Wang J, Fei G, Pan Y, Zhang K, Hao S, Zheng Z, Xia H (2019) Simultaneous reduction and surface functionalization of graphene oxide by cystamine dihydrochloride for rubber composites.Compos Part A: Appl Sci 122:18−26

20. Zou H, Wu S, Shen J (2008) Polymer/silica nanocomposites: preparation, characterization, properties, and applications. Chem Rev 108:3893–3957

21. Lee DW, Yoo BR (2016) Advanced silica/polymer composites: materials and applications. J Ind Eng Chem 38:1–12

22. Vo LT, Anastasiadis SH, Giannelis EP (2011) Dielectric study of poly(styrene-co-butadiene) composites with carbon black, silica, and nanoclay. Macromolecules 44:6162−6171
23. Nan C-W, Shen Y, Ma J (2010) Physical properties of composites near percolation. Ann Rev Mater Res 40:131–151
24. Dang ZM, Yuan JK, Yao SH, Liao RJ (2013) Flexible nanodielectric materials with high permittivity for power energy storage. Adv Mater 25:6334–6365
25. Dang ZM, Yuan JK, Zha J-W, Zhou T, Li S-T, Hu G-H (2012) Fundamentals, processes and applications of high-permittivity polymer–matrix composites. Prog Mater Sci 57:660–723
26. Wang B, Huang W, Chi L, Al-Hashimi M, Marks TJ, Facchetti A (2018) High-k gate dielectrics for emerging flexible and stretchable electronics. Chem Rev 118:5690–5754
27. Zhang Y, Qiu M, Yu Y, Wen B, Cheng L (2017) A novel polyaniline-coated bagasse fiber composite with core–shell heterostructure provides effective electromagnetic shielding performance. ACS Appl Mater Interfaces 9:809–818
28. Zhang QM, Li H, Poh M, Xia F, Cheng ZY, Xu H, Huang C (2020) An all-organic composite actuator material with a high dielectric constant. Nat 419:284–287
29. Li B, Randall CA, Manias E (2021) Submitted Manuscript
30. He F, Lau S, Chan HL, Fan J (2009) High dielectric permittivity and low percolation threshold in nanocomposites based on poly(vinylidene fluoride) and exfoliated graphite nanoplates. Adv Mater 21:710–715
31. Shen Y, Lin Y, Li M, Nan C-W (2007) High dielectric performance of polymer composite films induced by a percolating interparticle barrier layer. Adv Mater 19:1418–1422
32. Li B, Sarkarat M, Baker A, Randall CA, Manias E (2021) Interfacial effects on the dielectric properties of elastomer/carbon-black/ceramic composites. MRS Adv 6:247–251
33. Ryan DE, Manias E, Li B (2019) Elastomer composites with high dielectric constant. U.S. Patent 10,438,717, 8 Oct 2019
34. Litvinov VM, Orza RA, Klüppel M, van Duin M, Magusin PCMM (2011) Rubber–filler inter-actions and network structure in relation to stress–strain behavior of vulcanized, carbon black filled EPDM. Macromolecules 44:4887–4900
35. Stauffer D, Aharony A (1991) Introduction to percolation theory. Taylor & Francis, London
36. Bunde A, Havlin S (2012) Fractals and disordered systems. Springer, New York
37. Vega GFH (2019) Quantifying matrix complexity with the calculation of fractal dimensions from GC×GC chromatograms—a potential oil fingerprinting technique. Master Dissertation, Saint Mary's University
38. Captur G, Muthurangu V, Cook C, Flett AS, Wilson R, Barison A, Sado DM, Anderson S, McKenna WJ, Mohun TJ, Elliott PM (2013) Quantification of left ventricular trabeculae using fractal analysis. J Cardiovasc Magn Reson 15:36
39. Kalmykov YP, Coffey WT, Crothers DSF, Titov SV (2004) Microscopic models for dielectric relaxation in disordered systems. Phys Rev E 70:041103
40. Pötschke P, Dudkin SM, Alig I (2003) Dielectric spectroscopy on melt processed polycarbonate-multiwalled carbon nanotube composites. Polymer 44:5023–5030
41. Meier JG, Klüppel M (2008) Carbon black networking in elastomers monitored by dynamic mechanical and dielectric spectroscopy. Macromol Mater Eng 293:12–38
42. Meier JG, Mani JW, Klüppel M (2007) Analysis of carbon black networking in elastomers by dielectric spectroscopy. Phys Rev B 75:054202
43. Gefen Y, Aharony A, Alexander S, Anomalous S (1983) Diffusion on percolating clusters. Phys Rev Lett 50:77–80
44. Sidebottom DL (2009) Colloquium: understanding ion motion in disordered solids from impedance spectroscopy scaling. Rev Mod Phys 81:999–1014
45. Okamoto T, Long J, Wilkie R, Stitt J, Maier R, Randall CA (2016) A charge-based deep level transient spectroscopy measurement system and characterization of a ZnO-based varistor and a Fe-doped $SrTiO_3$ dielectric. Jap J Appl Phys 55:026601
46. Jones TB (1995) Electromechanics of particles. Cambridge University Press, New York